Partial spectral and temporal coherence of plane-wave pulse trains in second-harmonic generation

IOP Publishing Journal of Optics
J. Opt. **24** (2022) 025501 (9pp) https://doi.org/10.1088/2040-8986/ac3f94

Partial spectral and temporal coherence of plane-wave pulse trains in second-harmonic generation

Henri Pesonen*, Juha-Matti Huusko, Xiaorun Zang, Ari T Friberg, Jari Turunen and Tero Setälä

Institute of Photonics, University of Eastern Finland, PO Box 111, FI-80101 Joensuu, Finland

E-mail: henri.a.pesonen@uef.fi

Received 31 August 2021, revised 25 November 2021
Accepted for publication 2 December 2021
Published 4 January 2022

Abstract

We study the spectral and temporal coherence effects in the passage of a Gaussian Schell-model (GSM) scalar, plane-wave pulse train through a slab of nonlinear optical crystal exhibiting second-harmonic generation. We show that due to the nonlinear interaction the temporal and spectral degrees of coherence of the fundamental (F) and second-harmonic (SH) pulse trains at the exit facet may deviate markedly from the GSM and the global degree of coherence of the SH wave generally decreases with increasing incident F beam intensity. In addition, we find that due to the partial coherence of the incident GSM field the transmitted SH wave may show a double-peaked intensity distribution.

Keywords: coherence, second-harmonic generation, pulses, SHG

(Some figures may appear in colour only in the online journal)

1. Introduction

Coherent pulse trains of light, with each individual pulse having the same wave form, have significant applications in probing and manipulation of atoms and molecules, precision frequency metrology, telecommunications, micromachining, etc [1, 2]. However, any pulse-to-pulse variations in the pulse train render the averaged field to be partially coherent in both spectral and temporal domains [3], which necessitates a statistical analysis based on the second-order coherence theory of light. This involves concepts such as the two-frequency cross-spectral density (CSD) in the spectral domain and the two-time mutual coherence function (MCF) in the temporal domain. A great number of models [4] have been developed to describe spectrally and temporally partially coherent beams of pulsed light since the importance of the subject was recognized [5–7]. Recently, the field has expanded to cover the pulse trains especially in the contexts of supercontinuum (SC) light [8–10] and free-electron lasers [11–14].

In general, the effect of pulse train coherence of the incident (pump) beam on the various nonlinear material interactions has not been widely considered. For instance, in all studies on SC generation with photonic crystal fibers or bulk materials [15], coherent input illumination (with quantum noise) has always been taken. In this paper we will lift this assumption by letting the illuminating field be inherently partially coherent and investigate the ensuing effects on the interaction of pulse trains with nonlinear media.

A particularly important nonlinear optical effect is second-harmonic generation (SHG), with applications in, e.g. spectroscopy and remote sensing [16]. Previous studies concerning coherence and SHG relate to the SHG efficiency [17–19] and the influence of incoherence on the produced spectrum [20, 21]. Recently, the spatial coherence properties of the involved fundamental (F) and second-harmonic (SH) waves were considered in the context of stationary fields whose spectral components are necessarily uncorrelated [22].

In this work, we analyze the effect of spectral and temporal partial pulse-train coherence on SHG in a slab of optically nonlinear material. The incident field is taken to be a Gaussian

* Author to whom any correspondence should be addressed.

Schell-model (GSM) plane-wave pulse train whose spectral (and temporal) coherence width to pulse width ratio is kept fixed and the peak intensity varied. We demonstrate that the nonlinear interaction renders the transmitted F and SH waves different from the GSM. Further, increasing the peak intensity of the incident beam decreases the overall (global) spectral and temporal degrees of coherence of the SH field and in some cases emerges a two-peaked temporal intensity profile.

The structure of this work is as follows. In section 2 we introduce the concepts of optical coherence theory which are relevant for this work, while in section 3 the GSM pulse trains are described. In section 4 the spectral and temporal coherence properties of the F and SH pulse trains transmitted through an SHG material slab are assessed. Finally, section 5 summarizes the main results. In addition, appendix contains a derivation of the coupled wave equations related to the SHG and describes the Runge–Kutta method for their solution.

2. Description of pulse-train coherence

We begin by recalling the relevant concepts of the scalar-field coherence theory in the spectral and temporal domains. The CSD function $W(\omega_1,\omega_2)$ measures correlations between two angular frequencies ω_1 and ω_2 and is defined as an average over scalar electric field realizations $E(\omega)$, via [23]

$$W(\omega_1,\omega_2) = \langle E^*(\omega_1)E(\omega_2)\rangle, \tag{1}$$

where the asterisk denotes complex conjugation and the angle brackets ensemble averaging. As is customary the realizations are expressed in terms of complex analytic signals. In the context of pulse trains the realizations correspond to the individual pulses and in numerical computations a finite (large) number N of them is included in the average. By setting $\omega_1 = \omega_2 = \omega$ one attains the average spectral density $S(\omega)$ which can further be used to normalize the CSD and define the complex degree of spectral coherence

$$\mu(\bar{\omega},\Delta\omega) = \frac{W(\bar{\omega},\Delta\omega)}{\sqrt{S(\bar{\omega}-\Delta\omega/2)S(\bar{\omega}+\Delta\omega/2)}}, \tag{2}$$

where we have used average $\bar{\omega} = (\omega_1+\omega_2)/2$ and difference $\Delta\omega = \omega_2-\omega_1$ coordinates. In a similar fashion, one can investigate the correlations in the temporal domain by employing the Fourier transform

$$E(t) = \int_0^\infty E(\omega)\exp(-i\omega t)\mathrm{d}\omega, \tag{3}$$

on every realization and then averaging to obtain the two-time MCF

$$\Gamma(t_1,t_2) = \langle E^*(t_1)E(t_2)\rangle. \tag{4}$$

One may normalize the MCF by the average intensity $I(t) = \Gamma(t,t)$ and get the temporal degree of coherence that reads in the average $\bar{t} = (t_1+t_2)/2$ and difference $\Delta t = t_2-t_1$ coordinates as

$$\gamma(\bar{t},\Delta t) = \frac{\Gamma(\bar{t},\Delta t)}{\sqrt{I(\bar{t}-\Delta t/2)I(\bar{t}+\Delta t/2)}}. \tag{5}$$

In many cases the degree of coherence is not constant over the pulse and a more practical way to quantify the coherence state of a pulse train is to use the overall degree of coherence. In the spectral and temporal domains the square of this quantity reads, respectively, as [7]

$$\bar{\mu}^2 = \frac{\int_{-\infty}^{\infty}\int_0^\infty |W(\bar{\omega},\Delta\omega)|^2\mathrm{d}\bar{\omega}\mathrm{d}\Delta\omega}{\int_{-\infty}^{\infty}\int_0^\infty S(\bar{\omega}-\Delta\omega/2)S(\bar{\omega}+\Delta\omega/2)\mathrm{d}\bar{\omega}\mathrm{d}\Delta\omega}, \tag{6}$$

$$\bar{\gamma}^2 = \frac{\int_{-\infty}^{\infty}\int_{-\infty}^{\infty} |\Gamma(\bar{t},\Delta t)|^2\mathrm{d}\bar{t}\mathrm{d}\Delta t}{\int_{-\infty}^{\infty}\int_{-\infty}^{\infty} I(\bar{t}-\Delta t/2)I(\bar{t}+\Delta t/2)\mathrm{d}\bar{t}\mathrm{d}\Delta t}. \tag{7}$$

These parameters obey $\bar{\mu} = \bar{\gamma}$ and $0 \leqslant \bar{\mu},\bar{\gamma} \leqslant 1$.

Additional physical insight into the properties of a pulse train is obtained by investigating the coherence width to pulse width ratio. First, one may use the second moment to assess the effective spectral width, σ_s, as

$$\sigma_\mathrm{s}^2 = \frac{\int_0^\infty(\omega-\omega_0)^2S(\omega)\mathrm{d}\omega}{\int_0^\infty S(\omega)\mathrm{d}\omega}, \tag{8}$$

$$\omega_0 = \frac{\int_0^\infty \omega S(\omega)\mathrm{d}\omega}{\int_0^\infty S(\omega)\mathrm{d}\omega}. \tag{9}$$

Second, we define an integrated measure for the degree of spectral coherence

$$\mu_\mathrm{int}(\bar{\omega}) = \int_{-\infty}^{\infty}\mu(\bar{\omega},\Delta\omega)\mathrm{d}\Delta\omega, \tag{10}$$

and introduce the spectral density weighted effective coherence width

$$\Sigma_\mu = \frac{\int_0^\infty |\mu_\mathrm{int}(\omega)|S(\omega)\mathrm{d}\omega}{\int_0^\infty S(\omega)\mathrm{d}\omega}. \tag{11}$$

This formula emphasizes the degree of coherence at frequencies with significant spectral density. The width ratio $\Sigma_\mu/\sigma_\mathrm{s}$ then is a measure for the extent of correlations within the spectral band of the field. In a similar fashion one could define the effective pulse duration, the effective coherence time, and their ratio in the time domain. Width ratios defined in this way offer more intuitive information on the coherence characteristics of the field than the overall quantities $\bar{\mu}$ and $\bar{\gamma}$, at least in the sense that they can be seen as extensions of the width ratios into fields that are not of GSM type.

3. Gaussian Schell-model pulse trains

The GSM pulse trains constitute a special type of fields whose spectral density and degree of coherence are Gaussian functions and the latter depends only on the separation $\Delta\omega$ of the two frequencies. The CSD of a GSM plane-wave pulse train propagating along the z axis has (at $z=0$ plane) the form [7]

$$W(\bar{\omega},\Delta\omega) = S_0\,\exp\left[-\frac{(\bar{\omega}-\omega_0)^2}{2\sigma_\mathrm{s}^2} - \frac{1}{2}\left(\frac{1}{4\sigma_\mathrm{s}^2}+\frac{1}{\sigma_\mu^2}\right)\Delta\omega^2\right], \tag{12}$$

where S_0 is the peak spectral density and σ_μ characterizes the spectral coherence width. The spectral density is given by

$$S(\omega) = S_0 \exp\left[-\frac{(\omega-\omega_0)^2}{2\sigma_s^2}\right], \tag{13}$$

whereas the degree of coherence defined in equation (2) is

$$\mu(\Delta\omega) = \exp\left(-\frac{\Delta\omega^2}{2\sigma_\mu^2}\right). \tag{14}$$

Thus the parameters σ_s and σ_μ are the (normalized) rms widths of the spectrum and spectral coherence, respectively, associated with a pulsed GSM-type field. The width σ_s is consistent with equation (8) while Σ_μ of equation (11) satisfies $\Sigma_\mu = \sqrt{2\pi}\sigma_\mu$.

Using equations (1), (3), and (4) together with equation (12) one finds that the MCF of a GSM pulse train is

$$\Gamma(\bar{t},\Delta t) = I_0 \exp\left[-\frac{\bar{t}^2}{2T^2} - \frac{1}{2}\left(\frac{1}{4T^2}+\frac{1}{T_c^2}\right)\Delta T^2\right] \times \exp(-i\omega_0\Delta t), \tag{15}$$

where $I_0 = 4\pi S_0\sigma_\mu\sigma_s^2(\sigma_\mu^2+4\sigma_s^2)^{-1/2}$. The average intensity and the complex degree of temporal coherence are therefore given by

$$I(t) = I_0 \exp\left(-\frac{t^2}{2T^2}\right), \tag{16}$$

$$\gamma(\Delta t) = \exp\left(-\frac{\Delta t^2}{2T_c^2}\right)\exp(-i\omega_0\Delta t), \tag{17}$$

where

$$T = (\sigma_\mu^2+4\sigma_s^2)^{1/2}/2\sigma_s\sigma_\mu, \tag{18}$$

$$T_c = \sigma_\mu T/\sigma_s, \tag{19}$$

are the average pulse duration and the coherence time, respectively.

The CSD function in equation (12) admits a coherent-mode decomposition which in ω_1,ω_2 coordinates reads as

$$W(\omega_1,\omega_2) = \sum_{m=0}^{\infty}\alpha_m\psi_m^*(\omega_1)\psi_m(\omega_2), \tag{20}$$

where α_m and $\psi_m(\omega)$ are, respectively, the eigenvalues and the orthonormal eigenfunctions of a homogeneous Fredholm integral equation with the CSD as a kernel [23]. For a GSM pulse train the eigenfunctions are Hermite–Gaussian (HG) functions [7]

$$\psi_m(\omega) = \frac{1}{\sqrt{2^m m!}}\left(\frac{2e}{\pi}\right)^{1/4} H_m\left[\sqrt{2e}(\omega-\omega_0)\right] \times \exp[-e(\omega-\omega_0)^2], \tag{21}$$

where $H_m(\omega)$ are Hermite polynomials, $e = (a^2+2ab)^{1/2}$, $a = 1/4\sigma_s^2$, and $b = 1/2\sigma_\mu^2$. The weights are given by

$$\alpha_m = S_0\left(\frac{\pi}{a+b+e}\right)^{1/2}\left(\frac{b}{a+b+e}\right)^m. \tag{22}$$

We notice that the eigenfunctions and eigenvalues are real for a GSM beam (at the waist).

4. Effects of SHG on the coherence properties

In the following, we apply the above formalism to analyze the spectral and temporal coherence properties of the F and SH pulse trains at the output of a slab of nonlinear optical material exhibiting SHG.

4.1. Parameters of the SHG slab and the incident field

The slab has a thickness of $L = 15$ μm and an infinite transverse extent. We remark that thin films with a few micrometer (or even less than wavelength) thicknesses and supporting SHG have been employed in the context of epsilon-near-zero materials [24], two-dimensional atomic crystals [25], and ultrashort pulses [26]. We take the refractive index to be $n = 1.6$ for both F and SH waves. This choice together with the short propagation distance conforms to phase matching of the waves. Furthermore, the nonlinear coupling coefficient (susceptibility in contracted notation) is chosen as $d = 2.0$ pm V^{-1}. The entrance facet of the slab is set to be at the $z = 0$ plane and is illuminated by a GSM pulse train whose average spectrum, given in equation (13), is centered at $\omega_0 = 3.142$ rad fs^{-1} (corresponding to the wavelength of 600 nm) and has the rms width of $\sigma_s = 0.010$ rad fs^{-1}.

Throughout the work we choose the spectral coherence width in equation (14) as $\sigma_\mu = 0.7\sigma_s$. The pulse train therefore is spectrally rather (but not fully) coherent, and a few lowest-order modes dominate the coherent-mode decomposition of equation (20). More specifically, the ratios of the four lowest-order eigenvalues are given by $\alpha_1/\alpha_0 \approx 0.50$, $\alpha_2/\alpha_0 \approx 0.25$, and $\alpha_3/\alpha_0 \approx 0.13$. Hence, the energy of an individual realization is distributed essentially among a few lowest order modes. The modes with $m = 1,2,3$ possess amplitude peaks symmetrically around the center and this feature reflects (also after the mode-construction procedure described in section 4.2) in the spectral and temporal realizations which have high-amplitude peaks (nonsymmetrically) on both sides of the center of average pulse. Further, equations (18) and (19) indicate, respectively, that the average temporal length of the pulse train is $T = 151$ fs and the coherence time is $T_c = 0.7T$. In the numerical computations that follow, all coherence widths are fixed but the peak spectral density S_0 of the incident GSM pulse train varies.

4.2. Construction and propagation of realizations

We represent the GSM field by an ensemble of $N = 500$ realizations (pulses), each of which is transmitted through a slab of nonlinear optical crystal. We checked that this number ensures the convergence of the results. The procedure for generating

the ensemble is analogous to that described in [22] in the spatial domain. In short, a realization is expressed in terms of the HG modes in equation (21) with random coefficients and they are required to lead to the coherent-mode representation of equation (20). It follows that the relative weights of the HG modes constituting a realization are approximately given by $\sqrt{\alpha_m/\alpha_0}$, showing that in the arrangement considered in this work the three lowest order HG modes (with random phases) are dominant. However, we included the 50 lowest-order modes in the computations in order to ensure accuracy. We remark that several different ensembles can be generated which all represent the same incident GSM field. The various ensembles composed of different realizations then lead to different sets of the F and SH field realizations at the output which, in principle, can display distinct coherence properties for a field at the exit facet. We analyzed this feature and found that the various ensembles effectively imply the same results if the number of realizations N is large and the value $N = 500$ that we use is sufficient. The analogous property but with spatial domain fields was assessed in [22].

Propagation of the F and SH pulses in a material slab is governed by the electromagnetic wave equations with nonlinear source polarizations corresponding to the SHG. These formulas are given in equation (A.1) of appendix. The nonlinear material interaction couples the two fields and induces energy transfer between them on propagation. We assume that the fields are linearly polarized in the same direction. Consequently, the F and SH fields obey the scalar wave equations, equations (A.5) and (A.6), respectively, where the material interaction is specified by the susceptibility d. The coupled scalar-field wave equations are solved with the Runge–Kutta (RK) algorithm. The development of the wave equations, underlying assumptions, and the RK method are described in appendix.

Figure 1 exemplifies, in the case of $\sqrt{S_0} = 2.6\ \mathrm{GV\,m^{-1}}$, the average spectral densities (thick red and blue curves) of (a) the incident GSM pulse train and the related transmitted (b) F, and (c) SH waves. The thin black curves refer to a single (typical) realization. The nonlinear crystal couples the F and SH pulses and transfers energy from the high-amplitude parts of an F realization to an SH realization. This is evident in figure 1 where in (c) the two amplitude peaks are located at frequencies which are two times larger than the frequencies of the two strongest F amplitude peaks in (a). As seen in (b) the amplitude of the F pulse at the corresponding locations has decreased in transmission. A similar effect takes place at the small side lobe on the left but the relative amount of transferred energy is smaller since the nonlinear material interaction is weaker at smaller field strengths. As expected, also the average spectral densities (thick curves) follow similar trends. We observe that the spectral density of the SH pulse train is centered exactly at $2\omega_0$ whereas its width is larger than that of the incident pulse train (note the different frequency scales in the figure). By using equation (8), the widths of the average spectra of the transmitted F and SH fields are found to be $\sigma_s = 0.011\ \mathrm{rad\,fs^{-1}}$ and $\sigma_s = 0.016\ \mathrm{rad\,fs^{-1}}$, respectively. Their ratios to the spectral width of the incident field are hence 1.1 and 1.6, respectively, which indicate that both spectra are

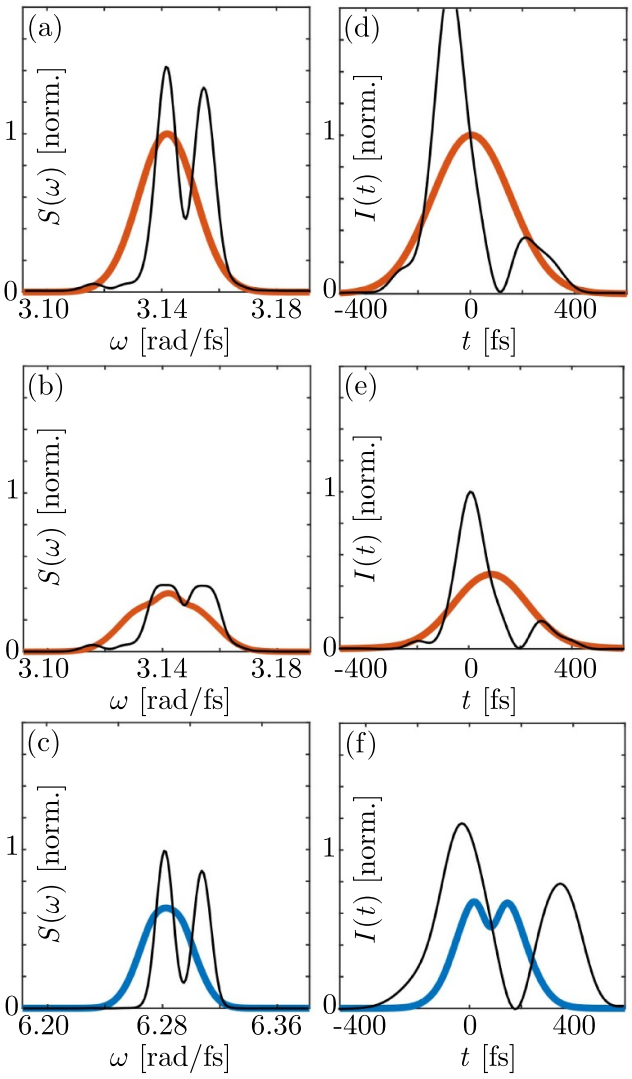

Figure 1. Illustration of typical spectral and temporal F and SH field realizations and the average spectral densities as well as intensities involved in SHG: ((a), (d)) incident GSM pulse train, ((b), (e)) transmitted F field, and ((c), (f)) transmitted SH field. The thick red and blue curves refer to the average quantities whereas the thin black curves correspond to a single realization. The incident-field and slab parameters are $\sigma_s = 0.010\ \mathrm{rad\,fs^{-1}}$, $\sigma_\mu = 0.7\sigma_s$, $\sqrt{S_0} = 2.6\ \mathrm{GV\,m^{-1}}$, $L = 15\ \mu\mathrm{m}$, and $d = 2.0 \times 10^{-12}\ \mathrm{m\,V^{-1}}$. The average spectral densities and temporal intensities have been normalized by the maximum value of the corresponding incident field quantity.

(effectively) wider than the incident one. The width values are strongly affected by the shape of the average spectrum which for both output fields deviate slightly from Gaussian showing that neither of them is a GSM pulse train.

Figures 1(d)–(f) show the temporal intensities related to the spectra in figures 1(a)–(c) obtained by Fourier transforming the individual realizations in terms of equation (3). The average intensities in ((e) and (f)) are centered at $t = 80$ fs corresponding to the propagation time through the slab. Part (f) demonstrates an important feature of two-peak formation in the average intensity which will be discussed in connection with figure 2(b).

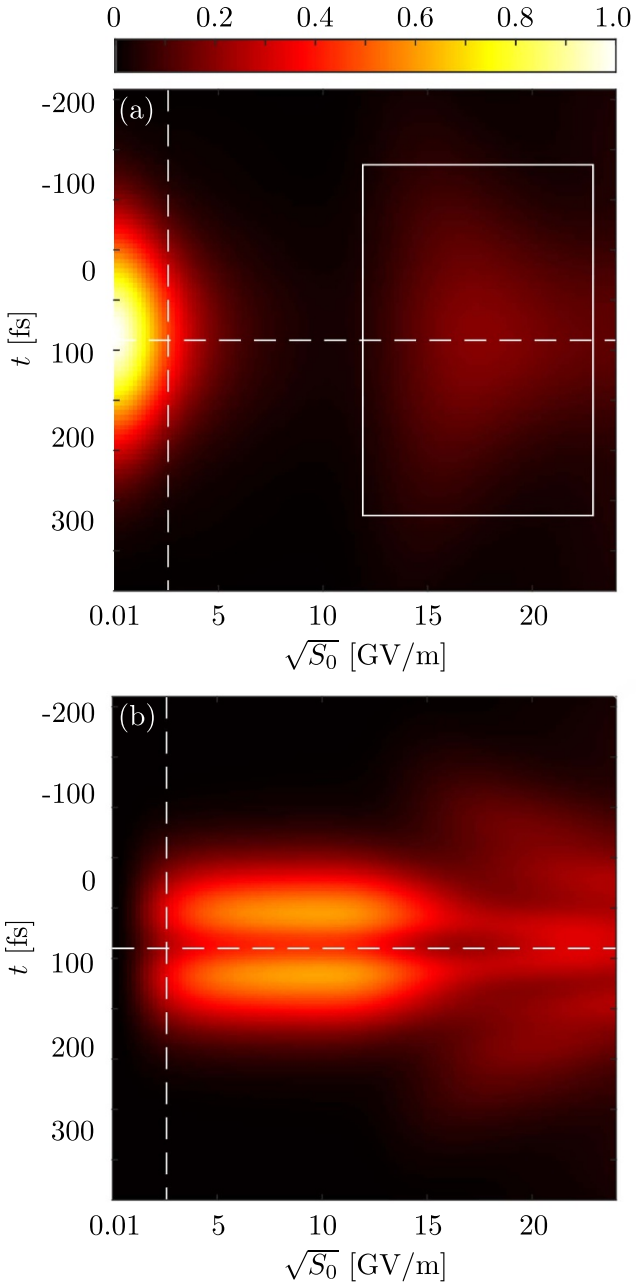

Figure 2. Average temporal intensities of the (a) F-wave and (b) SH-wave pulse trains at the output facet of the nonlinear material slab as a function of the incident GSM pulse train's peak amplitude. Otherwise the parameters of the incident field and the slab are as in figure 1. The dashed vertical line marks the case of $\sqrt{S_0} = 2.6\ \mathrm{GV\,m^{-1}}$ and the distributions have been normalized by I_0. The intensity distributions are centered at $t = 80$ fs (indicated by the dashed horizontal line) which corresponds to the propagation time through the slab. The rectangle in (a) emphasizes the region where the energy transfer from the SH wave back to the F field is strongest.

4.3. Effect of SHG on intensity

Figure 2 depicts the distributions of the average temporal intensities of the transmitted (a) F and (b) SH pulse trains as a function of the peak amplitude $\sqrt{S_0}$ of the incident field for the same parameters as used in figure 1. As an example, in the case of $\sqrt{S_0} = 2.6\ \mathrm{GV\,m^{-1}}$ (indicated by the dashed vertical line), the temporal rms widths of the incident F, transmitted F, and transmitted SH pulse trains are 151 fs, 149 fs, and 115 fs, respectively. The corresponding transmitted-to-incident pulse length ratios are 0.99 (F) and 0.76 (SH). A striking feature is seen in the shape of the SH pulse train in (b) where the intensity is double-peaked within the interval $2\ \mathrm{GV\,m^{-1}} \lesssim \sqrt{S_0} \lesssim 15\ \mathrm{GV\,m^{-1}}$. This effect of dual-peak formation in the SH wave train is related to partial coherence of the incident GSM pulse train. More precisely, as pointed out in section 4.1, the strongest amplitude peaks of a random-shaped temporal realization of the incident partially coherent field locate on the both sides of the center of the average pulse [see figure 1(d)]. As the realization propagates, SHG is strongest at the peak positions resulting in an SH realization whose intensity maxima are likewise located at both sides of the center [see the black curve in figure 1(e)]. This feature is reflected to the average SH pulse which is two-peaked. Further, the two-peak structure of the SH beam vanishes if the incident pulse train is fully coherent (all pulses are identical and Gaussian). Thus, adjusting the partial coherence of the incident pulse train (ratio of σ_s and σ_μ) may allow to tailor the average temporal shape of the train via a nonlinear material interaction. We further observe that, above $\sqrt{S_0} \approx 15\ \mathrm{GV\,m^{-1}}$, a significant amount of energy transfers back to the F wave. The region where the effect is strongest is highlighted by the rectangle.

4.4. Effect of SHG on temporal and spectral coherence

Next we consider the global coherence properties of the transmitted F and SH pulse trains. The overall degrees of coherence are shown in figure 3(a) as a function of $\sqrt{S_0}$. For reference, we illustrate in figure 3(b) typical F and SH realisations for the $\sqrt{S_0}$-values of 15 and 22 $\mathrm{GV\,m^{-1}}$ in the columns from left to right, respectively. From (a) we see that the coherence of the F pulse train decreases rapidly when the peak amplitude of the incident F wave is below $10\ \mathrm{GV\,m^{-1}}$. This behavior is related to the decrease of the strongest peaks in the F realizations in slab transmission as explained in connection with figure 1. The weakening of peaks, originating from the nonlinear interaction, levels the strength differences of the amplitude maxima in the realizations and hence increases the number of dominant peaks. This is observed in the black curve of figure 1(b). Consequently, the transmitted F pulses with increased structural complexity represent a field with decreased overall degree of coherence. Below $10\ \mathrm{GV\,m^{-1}}$ the overall degree of coherence of the SH wave is almost constant since the generated realizations are rather simple in shape as indicated by the black curve of figure 1(c). When the incident peak amplitude of the F wave exceeds $10\ \mathrm{GV\,m^{-1}}$, a significant amount of energy transfers from the SH field back to the F wave on propagation. In particular, the general behavior of the realizations above $10\ \mathrm{GV\,m^{-1}}$ is opposite to that below this level. More precisely, the energy transfer is strongest at the locations of the highest peaks of the SH realizations leveling the strength differences of the peaks [see the lower left plot in figure 3(b)]. Consequently, the degree of coherence decreases rapidly within $10\ \mathrm{GV\,m^{-1}} \lesssim \sqrt{S_0} \lesssim 17\ \mathrm{GV\,m^{-1}}$. We verified numerically

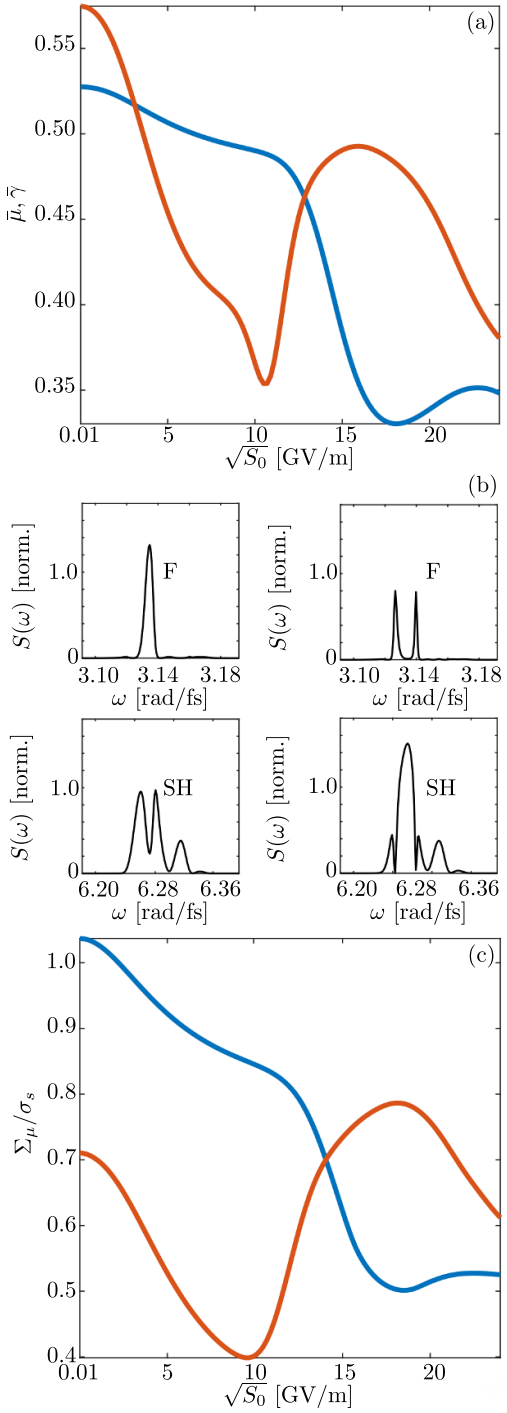

Figure 3. Illustration of the coherence properties related to the transmitted F (red curves) and SH (blue curves) pulse trains as a function of the incident GSM pulse train's peak amplitude. (a) The overall temporal and spectral degrees of coherence ($\bar{\mu} = \bar{\gamma}$), (b) the spectra of typical F and SH realizations for $\sqrt{S_0} =$ (15,22) GV m^{-1} corresponding to columns from left to right, and (c) coherence width to pulse width ratio. Apart from varying S_0 the parameters of the incident field and the slab are as in figure 1. The curves in (b) have been normalized by S_0.

that in this interval the F realizations take simpler forms, with essentially a single dominant peak [see the upper left figure in figure 3(b)], and hence the degree of coherence increases. Above 17 GV m^{-1} the energy transfer process between the F and SH waves is again reversed. In addition, the level of coherence decreases in both waves as indicated by the increased number of peaks in the realizations of the right column of (b). We remark that the above effects were found for a chosen L-value and with thicker slabs the effects would occur at lower incident intensities.

Besides the overall degree of coherence, an illustrative measure for the range of correlations (coherence) within the pulse train is the coherence width to pulse width ratio, Σ_μ/σ_s, which can be obtained from equations (8) and (11). This ratio for the transmitted F and SH pulses is shown in figure 3(b) with red and blue curves, respectively. The main features are the same as in (a). At this stage we summarize by noting that, within the considered amplitude range, the global coherence of the SH wave generally decreases at the exit facet whereas that of the F field oscillates with increasing incident field intensity.

Figures 4(a) and (b) show the spectral and temporal degrees of coherence, respectively, for the transmitted SH pulse train at $\sqrt{S_0} = 2.6$ GV m^{-1}. In the vicinity of $\bar{\omega} = 2\omega_0 = 6.284$ rad fs^{-1} the SH field deviates from the GSM type, for which the magnitude of the degree of coherence would be a horizontal bar in the average and difference frequency coordinates. At $\bar{\omega} = 2\omega_0$ the degree exhibits a modulation in the $\Delta\omega$ direction with minima at $\Delta\omega = \pm 0.016$ rad s^{-1}. A similar modulation effect as shown here for the SH field exists also in the transmitted F pulse train. In general, figure 4(a) demonstrates that for the transmitted SH field the spectral correlations around the center frequency extend farther than in the edge regions of the spectrum.

Also the temporal degree of coherence exhibits modulation as seen in figure 4(b). More precisely, the degree is modulated in the Δt direction close to $\bar{t} = 80$ fs (dashed line), which corresponds to the time of propagation through the slab, and assumes minimum value at $\Delta t = \pm 102$ fs. An essential feature is that the temporal degree of coherence deviates from the GSM form, for which the distribution would be horizontal bar whose width is specified by the temporal coherence width. In particular, close to $\bar{t} = 80$ fs, the temporal correlations extend farther that in the tail parts.

Figure 4 illustrates the particular case of $\sqrt{S_0} = 2.6$ GV m^{-1}, for which the intensity distribution exhibits the double-peak structure shown in figure 2. If the incident amplitude $\sqrt{S_0}$ is increased the modulation of the spectral and temporal degrees of coherence in figure 4 vanishes and the degrees become narrower around $\bar{\omega} = 2\omega_0$ and $\bar{t} = 80$ fs, respectively. This decreases the SH overall degrees of coherence in the two domains at high $\sqrt{S_0}$ values as observed in figure 3 above 10 GV m^{-1}.

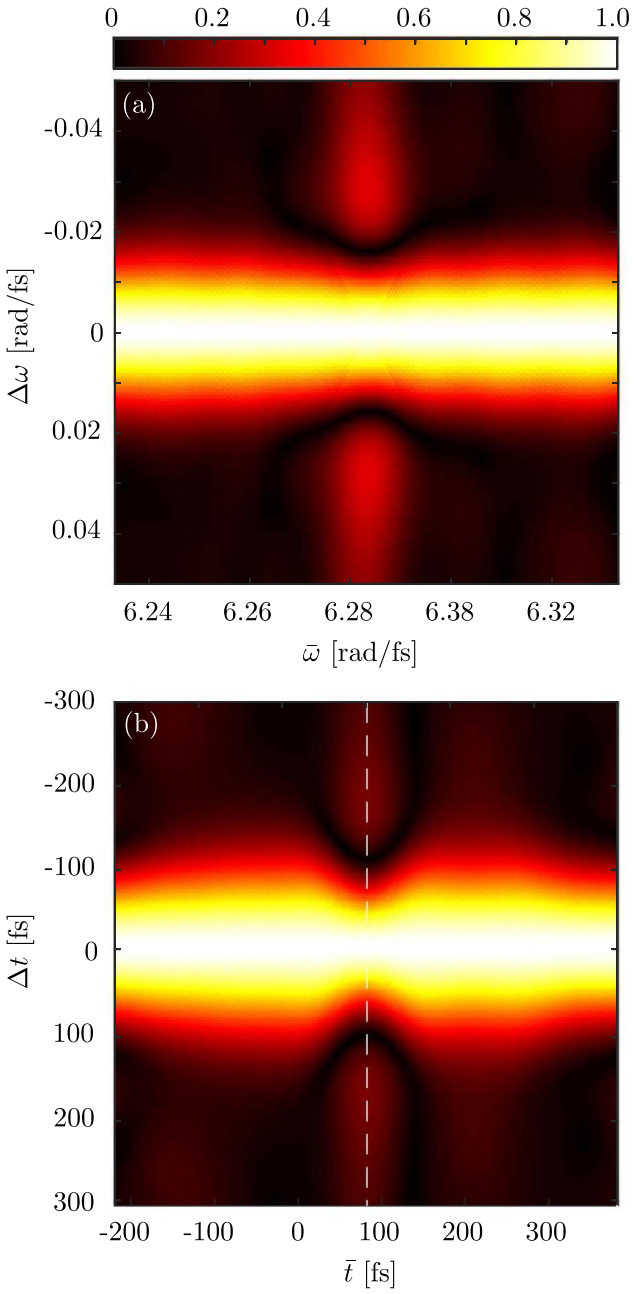

Figure 4. Distributions of the magnitudes of the degrees of coherence in (a) the spectral domain and (b) the temporal domain, of the transmitted SH field. The various geometry parameters are as in figure 1. The dashed line marks the location $\bar{t} = 80$ fs which corresponds to the propagation time through the slab. In the center region the spectral and temporal coherences are modulated in the $\Delta\omega$ and Δt directions, respectively, with minima at $\Delta\omega = \pm 0.016$ rad s^{-1} and $\Delta t = \pm 102$ fs.

5. Conclusions

As a summary, we considered an incident scalar, GSM plane-wave pulse train and evaluated the spectral and temporal coherence properties of the F and SH waves at the output facet of an optical crystal exhibiting SHG when the GSM peak amplitude was varied. Throughout the work the spectral (and temporal) coherence width to pulse width ratio of the incoming field was fixed at 0.7 indicating the we considered a rather coherent pulse train. We found that both transmitted beams, in general, may deviate essentially from the GSM as the correlation lengths within the pulse spectrum and temporal intensity vary. Further, the global degree of coherence of the F field at the output oscillates while that of the SH wave decreases with increasing incident intensity. We also found that for some input beam intensities partial coherence of the incident field induces a two-peak temporal intensity distribution for the SH field. The results of this work demonstrate that when SHG with a partially coherent pulse train is employed to produce light at frequencies which are not directly available or where efficient detectors exists the coherence properties may have a significant effect on the characteristics of the SH field.

Data availability statement

The data that support the findings of this study are available upon reasonable request from the authors.

Acknowledgments

Academy of Finland (projects 308393 and 310511). The work is part of the Academy of Finland Flagship Programme, Photonics Research and Innovation (PREIN, 320166).

Appendix. Coupled wave equations for the F and SH waves

We first derive the coupled wave equations for the fundamental (F) and the second-harmonic (SH) plane-wave pulse fields that govern their propagation in a material exhibiting second-harmonic generation. Along the derivation we highlight the underlying assumptions. At the end, we describe the Runge–Kutta (RK) method that was employed to solve the two equations.

As the F and SH light fields propagate their amplitudes are coupled by the induced nonlinear polarization. In general, the fields require electromagnetic treatment and hence we denote the electric fields of the F and SH spectral pulses by $\mathbf{E}_1(\mathbf{r},\omega_1)$ and $\mathbf{E}_2(\mathbf{r},\omega_2)$, respectively. Notice that the angular frequencies ω_1 and ω_2 refer to the F and SH waves and they should not be confused with the frequency arguments of the CSD in the main text. Both fields are plane-wave pulses and we set them to propagate along the z axis. We assume that the medium is homogeneous, nonmagnetic, contains no free charges and currents, and its linear response is local and isotropic with negligible dispersion. The behaviors of the two fields are in the spectral domain governed by the inhomogeneous wave equations [16]

$$\nabla\times\nabla\times\mathbf{E}_m(\mathbf{r},\omega_m) - k_m^2\mathbf{E}_m(\mathbf{r},\omega_m) = \mu_0\omega_m^2\mathbf{P}_m^{(\mathrm{NL})}(\mathbf{r},\omega_m), \quad m=(1,2), \tag{A.1}$$

where $\mathbf{r}$ refers to a point in space, $k_m = n\omega_m/c$ is the wave number at angular frequency ω_m with c being the vacuum speed of light, and μ_0 is the vacuum permeability. In addition, n is the refractive index which is set independent of frequency due to weak dispersion. Moreover, $\mathbf{P}_m^{(\mathrm{NL})}(\mathbf{r},\omega_m)$ is the nonlinear (source) polarization at frequency ω_m, whose $i=(x,y)$ component generally reads as

$$P_{mi}^{(\mathrm{NL})}(\mathbf{r},\omega_m) = \epsilon_0 \sum_{jk} \chi_{ijk}^{(2)}(\omega_m,\omega_a,\omega_b) E_j(\mathbf{r},\omega_a) E_k(\mathbf{r},\omega_b), \tag{A.2}$$

where $\chi_{ijk}^{(2)}(\omega_m,\omega_a,\omega_b)$ is the second-order nonlinear susceptibility with $\omega_m = \omega_a + \omega_b$. The quantities $E_j(\mathbf{r},\omega_a)$ and $E_k(\mathbf{r},\omega_b)$, with $(j,k)=(x,y)$, represent the Cartesian field components at frequencies ω_a and ω_b. For the SH field $\omega_m = \omega_2$, $\omega_a = \omega_b = \omega_1$ while for the F wave $\omega_m = \omega_1$, $\omega_a = \omega_2$, and $\omega_b = -\omega_1$ hold.

Next we take both fields to be linearly polarized in the x direction reducing the problem to a scalar-field case conforming to the theory of the main text. The source polarizations for the F and SH fields in equation (A.2) take the respective forms

$$P_1^{(\mathrm{NL})}(\mathbf{r},\omega_1) = 2\epsilon_0 \chi_{xxx}^{(2)}(\omega_1,\omega_2,-\omega_1) E_x(\mathbf{r},\omega_2) E_x^*(\mathbf{r},\omega_1), \tag{A.3}$$

$$P_2^{(\mathrm{NL})}(\mathbf{r},\omega_2) = \epsilon_0 \chi_{xxx}^{(2)}(\omega_2,\omega_1,\omega_1) E_x^2(\mathbf{r},\omega_1). \tag{A.4}$$

In equation (A.3) we used the intrinsic permutation symmetry of the susceptibility and the property $E_x(\mathbf{r},-\omega_1) = E_x^*(\mathbf{r},\omega_1)$. Assuming the Kleinmann symmetry condition and invoking the contracted notation $\chi_{xxx}^{(2)}(\omega_2,\omega_1,\omega_1) = 2d_{11} = 2d$, enables to develop the two wave equations in equation (A.1) into the form

$$\frac{\partial^2 E_1(z,\omega_1)}{\partial z^2} + k_1^2 E_1(z,\omega_1) = -4\frac{\omega_1^2 d}{c^2} E_1^*(z,\omega_1) E_2(z,\omega_2), \tag{A.5}$$

$$\frac{\partial^2 E_2(z,\omega_2)}{\partial z^2} + k_2^2 E_2(z,\omega_2) = -2\frac{\omega_2^2 d}{c^2} E_1^2(z,\omega_1). \tag{A.6}$$

Here we also used the fact that $\nabla \cdot \mathbf{E}_m(\mathbf{r},\omega_m) = 0$ holds for both $m=(1,2)$ since the fields are plane-wave pulses. In addition, we employed the invariance of the fields in the transverse direction and some basic properties of the nonlinear susceptibility. Notice that the reduction to the scalar-field case requires that the medium is such that d_{11} is the only significant element of the material's d matrix.

The numerical procedure of the F and SH wave propagation is based on the RK method [27] and is as follows. We first write $E_m(z,\omega_m) = A_m(z,\omega_m)\exp(ik_m z)$, $m=(1,2)$, and assume that the waves are phase matched obeying $\Delta k = k_2 - 2k_1 = 0$. Equations (A.5) and (A.6) thus transform into

$$\frac{\partial^2 A_1(z,\omega_1)}{\partial z^2} + 2ik_1 \frac{\partial A_1(z,\omega_1)}{\partial z} = -4\frac{\omega_1^2 d}{c^2} A_1^*(z,\omega_1) A_2(z,\omega_2), \tag{A.7}$$

$$\frac{\partial^2 A_2(z,\omega_2)}{\partial z^2} + 2ik_2 \frac{\partial A_2(z,\omega_2)}{\partial z} = -2\frac{\omega_2^2 d}{c^2} A_1^2(z,\omega_1). \tag{A.8}$$

Next we introduce a new variable $A'_m(z,\omega_m) = \partial A_m(z,\omega_m)/\partial z$ which allows us to split the above pair of equations as

$$\frac{\partial A_1(z,\omega_1)}{\partial z} = A'_1(z,\omega_1), \tag{A.9}$$

$$\frac{\partial A'_1(z,\omega_1)}{\partial z} = -2ik_1 A'_1(z,\omega_1) - 4\frac{\omega_1^2 d}{c^2} A_1^*(z,\omega_1) A_2(z,\omega_2), \tag{A.10}$$

$$\frac{\partial A_2(z,\omega_2)}{\partial z} = A'_2(z,\omega_2), \tag{A.11}$$

$$\frac{\partial A'_2(z,\omega_2)}{\partial z} = -2ik_2 A'_2(z,\omega_2) - 2\frac{\omega_2^2 d}{c^2} A_1^2(z,\omega_1). \tag{A.12}$$

This set of equations can be integrated with respect to z in terms of the RK algorithm.

The accuracy of the RK method was verified by COMSOL simulations which implied identical results. We used a two-dimensional model in the COMSOL analysis with the mesh element size down to $\lambda_1/50$. In brief, equation (A.1) at F and SH frequencies are coupled and solved under two electromagnetic waves, frequency domain (ewfd) interfaces [28]. Equations (A.3) and (A.4), respectively, are used to set the Polarization node under each ewfd interface for coupling the F and SH light fields.

We also point out that the commonly used slowly-varying envelope approximation (SVEA) [16], which we also tried in analogy with the spatial-domain analysis in [22], failed to predict the transfer of power back to the F wave after certain pump power levels ($\sqrt{S_0}$ above 15 GV m^{-1}, see figure 2). We therefore resorted to rigorous solutions of Maxwell's equations by the RK algorithm.

ORCID iD

Henri Pesonen https://orcid.org/0000-0001-5329-9577

References

[1] Saleh B E A and Teich M C 2007 *Fundamentals of Photonics* 2nd edn (Hoboken, NJ: Wiley)
[2] Trebino R 2000 *Frequency-Resolved Optical Gating: The Measurement of Ultrashort Laser Pulses* (Amsterdam: Kluwer Academic)
[3] Walmsley I A and Dorrer C 2009 Characterization of ultrashort electromagnetic pulses *Adv. Opt. Photonics* **1** 308–437
[4] Cai Y, Chen Y and Wang F 2014 Generation and propagation of partially coherent beams with nonconventional correlation functions: a review [invited] *J. Opt. Soc. Am.* A **31** 2083–96
[5] Christov I P 1986 Propagation of partially coherent light pulses *Opt. Acta* **33** 63–72
[6] Pääkkönen P, Turunen J, Vahimaa P, Friberg A T and Wyrowski F 2002 Partially coherent Gaussian pulses *Opt. Commun.* **204** 53–58

[7] Lajunen H, Tervo J and Vahimaa P 2004 Overall coherence and coherent-mode expansion of spectrally partially coherent plane-wave pulses *J. Opt. Soc. Am.* A **21** 2117–23
[8] Genty G, Surakka M, Turunen J and Friberg A T 2010 Second-order coherence of supercontinuum light *Opt. Lett.* **35** 3057–9
[9] Genty G, Surakka M, Turunen J and Friberg A T 2011 Complete characterization of supercontinuum coherence *J. Opt. Soc. Am.* B **28** 2301–9
[10] Närhi M, Turunen J, Friberg A T and Genty G 2016 Experimental measurement of the second-order coherence of supercontinuum *Phys. Rev. Lett.* **116** 243901
[11] Mitzner R *et al* 2008 Spatio-temporal coherence of free electron laser pulses in the soft x-ray regime *Opt. Express* **16** 19909–19
[12] Roling S, Siemer B, Wöstmann M, Zacharias H, Mitzner R, Singer A, Tiedtke K and Vartanyants I A 2011 Temporal and spatial coherence properties of free-electron laser pulses in the extreme ultraviolet region *Phys. Rev. Spec. Top. Accel. Beams* **14** 080701
[13] Vartanyants I A *et al* 2001 Coherence properties of individual femtosecond pulses of an x-ray free-electron laser *Phys. Rev. Lett.* **107** 144801
[14] Ahad L, Vartiainen I, Setälä T, Friberg A T, David C, Makita M and Turunen J 2016 On spectral and temporal coherence of x-ray free-electron laser beams *Opt. Express* **24** 13081–90
[15] Genty G, Friberg A T and Turunen J 2016 Coherence of supercontinuum light *Progress in Optics* vol 61, ed T Visser (Amsterdam: Elsevier) ch 2, pp 71–111
[16] Boyd R W 2008 *Nonlinear Optics* 3rd edn (New York: Academic)
[17] Zubairy M S and McIver J K 1987 Second-harmonic generation by a partially coherent beam *Phys. Rev.* A **36** 202–6
[18] Cai Y and Peschel U 2007 Second-harmonic generation by an astigmatic partially coherent beam *Opt. Express* **15** 15480–92
[19] Ji L *et al* 2019 High-efficiency second-harmonic generation of low-temporal-coherent light pulse *Opt. Lett.* **44** 4359–62
[20] Pyragaite V, Stabinis A and Piskarskas A 2012 Frequency spectrum of second-harmonic radiation exited by a Gaussian Schell-model beam *Phys. Rev.* A **86** 033812
[21] Stanislovaitis P, Narmontas A, Pyragaite V and Smilgevičius V 2014 Generation of a second-harmonic beam from incoherent conical beams *Phys. Rev.* A **89** 043821
[22] Pesonen H, Halder A, Huusko J–M, Friberg A T, Setälä T and Turunen J 2021 Spatial coherence effects in second-harmonic generation of scalar light fields *J. Opt.* **23** 035501
[23] Mandel L and Wolf E 1995 *Optical Coherence and Quantum Optics* (Cambridge: Cambridge University Press)
[24] Passler N C, Razdolski I, Katzer D S, Storm D F, Caldwell J D, Wolf M and Paarmann A 2019 Second harmonic generation from phononic epsilon-near-zero Berreman modes in ultrathin polar crystal films *ACS Photonics* **6** 1365–71
[25] Zhao M, Ye Z, Suzuki R, Ye Y, Zhu H, Xiao J, Wang Y, Iwasa Y and Zhang X 2016 Atomically phase-matched second-harmonic generation in a 2D crystal *Light Sci. Appl.* **5** e16131
[26] Sidick E, Knoesen A and Dienes A 1995 Ultrashort-pulse second-harmonic generation. I. Transform-limited fundamental pulses *J. Opt. Soc. Am.* B **12** 1704–12
[27] Butcher J C 2016 *Numerical Methods for Ordinary Differential Equations* 3rd edn (Hoboken, NJ: Wiley)
[28] COMSOL Multiphysics v. 5.5. COMSOL AB 2019 *Wave Optics Module User's Guide* (Stockholm, Sweden) pp 70–113